Available online at www.sciencedirect.com
ScienceDirect
Advances in Space Research 46 (2010) 557–570
ADVANCES IN SPACE RESEARCH (a COSPAR publication)
www.elsevier.com/locate/asr

MCAV/IMU integrated navigation for the powered descent phase of Mars EDL

Li Shuang [a,*], Peng Yuming [a], Lu Yuping [a], Zhang Liu [b], Liu Yufei [c]

[a] College of Astronautics, Nanjing University of Aeronautics and Astronautics, Nanjing 210016, China
[b] Changchun Institute of Optics, Fine Mechanics and Physics, Chinese Academy of Sciences, Changchun 130033, China
[c] P.O. Box 5142-109, China Academy of Space Technology, Beijing 100094, China

Received 22 December 2009; received in revised form 20 April 2010; accepted 21 April 2010

Abstract

Pin-point landing is considered as a key technology for future manned Mars landing and Mars base missions. The traditional inertial navigation system (INS) based guidance, navigation and control (GNC) mode used in the Mars entry, descent and landing (EDL) phase has no ability to achieve the precise and safe Mars landing, so novel EDL GNC methodologies should be investigated to meet this goal. This paper proposes the MCAV/IMU integrated navigation scheme for the powered descent phase of Mars EDL. The Miniature Coherent Altimeter and Velocimeter (MCAV) is adopted to correct the inertial bias and drift and improve the performance of integrated navigation. Altitude and velocity information derived from MCAV and the lander's state information sensed by inertial measurement unit (IMU) are integrated in extended Kalman filter algorithm. The validity of the proposed navigation scheme is confirmed by computer simulation.

Keywords: Integrated navigation; Mars powered descent; MCAV; Extended Kalman filter

1. Introduction

All Mars landers to date continue to rely on the entry, descent and landing (EDL) technologies developed for the Viking missions in the mid-seventies of the last century. At the same time, almost all Mars landers, except for 2008 Phoenix lander, perform the same EDL operations with the following sequence: entering the atmosphere on a ballistic trajectory, deploying a parachute while traveling at supersonic speeds and using airbags to survive the impact on the surface of the planet. Viking-like landers adopt inertial measurement unit (IMU) based navigation mode and unguided ballistic trajectory entry without life control, which lead to larger landing error ellipse and lower altitude landing site restriction (Wolf et al., 2005; Brand et al., 2004; Korzun et al., 2009; Li and Zhang, 2009; Burkhart et al., 2001; Benjamin et al., 1997; Cheng and Developme, 2006; Braun and Manning, 2007). With the lapse of time and the advances of technologies, estimated Mars landing accuracy to date has gradually improved from ~150 km of Mars pathfinder to ~35 km for the Mars exploration rovers to 10 km for 2011 Mars Science Laboratory (MSL) (Wolf et al., 2005; Korzun et al., 2009; Way et al., 2007). It is believed that MSL is challenging the capabilities of Viking-heritage EDL technologies, defining an upper bound on the performance of the first generation EDL systems and GNC mode (Way et al., 2007; Striepe et al., 2006; Steltzner et al., 2006).

Future Mars missions, such as Mars sample return, manned Mars landing and Mars base, need to achieve the pin-point Mars landing (safe landing within tens of meters to 100 m of a preselected target site) (Brand et al., 2004; Singh, 2007). The meanings of pin-point landing are two-fold. First, the landing accuracy is no larger than

* Corresponding author. Tel.: +86 25 84896520.
E-mail address: lishuang@nuaa.edu.cn (S. Li).

0273-1177/$36.00 © 2010 COSPAR. Published by Elsevier Ltd. All rights reserved.
doi:10.1016/j.asr.2010.04.028

100 m. Second, the landers should have the ability to automatically avoid the potential obstacles near the selected landing site (Li and Zhang, 2009). Since, the current EDL system and GNC methods cannot satisfy the requirements for future pin-point Mars landing missions, the next generation of EDL system and GNC methodologies are required in order to deliver the largest and most capable lander/rover to date to the surface of Mars. NASA has sought for the advanced entry, descent and landing (EDL) technologies to achieve pin-point landing, which includes hypersonic guided entry, high-precision EDL relative navigation technology, Mars Guided Parachute, sky crane terminal descent and autonomous hazard detection and avoidance (Wolf et al., 2005; Brand et al., 2004; Korzun et al., 2009; Burkhart et al., 2001; Benjamin et al., 1997; Cheng and Developme, 2006; Braun and Manning, 2007; Way et al., 2007; Striepe et al., 2006; Steltzner et al., 2006; Singh, 2007). European Space Agency (ESA) fastens much attention on developing the advanced EDL navigation guidance and control technology as well. In the frame of Aurora exploration program, the high fidelity end-to-end entry, descent and landing simulator (EAGLE) and the Precision Landing GNC Test Facility (PLGTF) have been set up to validate and verify the autonomous safe precision landing GNC technologies, both vision and LIDAR based, in a realistic environment (Guizzo et al., 2007; Alain, 2008; Parreira et al., 2007; Rogata et al., 2007). China has already initiated the technical preparation for post-"YH-1" era Mars landing and sample return exploration missions (Li, 2009; Li et al., 2007).

With the support of National Natural Science Foundation of China (NSFC) and China Academy of Space Technology (CAST), we have been working to develop the innovative EDL GNC scheme and detailed navigation and guidance algorithms for every phases of Mars EDL. In this paper, we propose and implement MCAV/IMU integrated navigation for the powered descent phase of Mars EDL. MCAV is adopted to correct the inertial bias and drift and improve the performance of navigation algorithm. Altitude and velocity information derived from MCAV and the lander state information sensed by IMU are integrated in extended Kalman filter algorithm to obtain the optimal state estimation. At the same time, data from other GNC sensors, such as lidar or radar, can be easily included in the filter to improve the lander state estimation (Parkes and Silva, 2001).

This paper is structured as follows. Section 2 briefly describes the representative Mars entry, descent, and landing (EDL) scenario. Section 3 defines the necessary coordinate system and coordinate transformation matrix used in the MCAV/IMU integrated navigation. Section 4 introduces the new-style navigation sensor MCAV. IMU model and Mars landing dynamic equations are defined in Section 5. MCAV/IMU integrated navigation algorithm is designed at length in Section 6. In Section 7, simulation system compositions are described and results are discussed as well. Finally, Section 8 contains conclusion.

2. Mars EDL sequence overview

Mars entry, descent and landing (EDL) phase is the most critical portion of the Mars landing exploration mission and whether it successes or not directly determines the success or failure of the entire Mars exploration mission. The entry vehicle separates from the cruise stage tens of minutes before the start-up of the final entry, descent and landing (EDL). The EDL sequence begins at Mars atmosphere interface (defined as a radius of 3522 km from the center of Mars) and ends with a safe touchdown, which includes hypersonic entry phase, parachute descent phase and powered descent phase (Burkhart et al., 2001; Li, 2009). Fig. 1 shows the sequence of events for the future representative Mars EDL baseline scenario.

The hypersonic entry phase will start, when the entry vehicle arrives at Mars atmosphere interface. In order to achieve the smaller error ellipse and landing spacecraft at higher latitude region, the closed-loop GNC system is used guide the entry vehicle through the hypersonic phase to the supersonic flight phase. The future Mars lander will adopt the lifting entry body configuration (achieved via center of gravity offset from center of pressure) and control the orientation of the lift vector by bank angle modulation. This is very different from the Viking-era landers, which all have performed zero-life ballistic entry, descent and landing and led to larger landing errors.

Once specified threshold (such as Mach number and altitude) are met after the hypersonic entry phase, the supersonic parachute is deployed. The parachute phase begins at the moment when the supersonic parachute is deployed. Additional criteria are also defined to release the supersonic parachute and deploy the subsonic parachute. Once the subsonic parachute deployment conditions are achieved, the backshell is released to allow the subsonic parachute

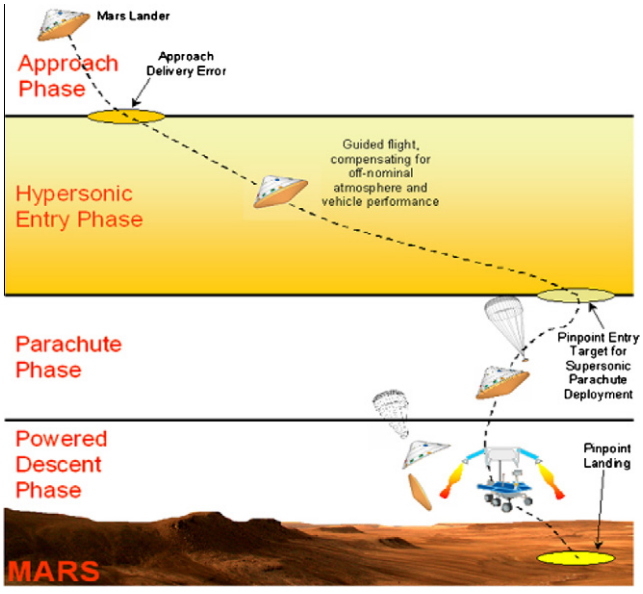

Fig. 1. Representative entry, descent, and landing (EDL) scenario.

to be deployed. Almost at the same time, the heat shield automatically separates from the lander and landing sensors and actuators are exposed.

The subsonic parachute deployment marks the beginning of the powered descent phase. Since both navigation sensors (radar or LIDAR) and actuators (thrusters) begin to work in this phase, the lander has the capability of high precision relative navigation and autonomous obstacle detection and avoidance. The main objectives of the powered descent phase have two aspects, one goal is lowering down the lander's velocity so as to achieve the soft landing, another is selecting suitable landing site and avoiding the potential obstacles in the course of landing.

3. Coordinate systems and transformation matrix

As relative geometrical relationship and coordinate transformation matrix between the navigation sensor MCAV and the surface of Mars play an essential role in designing the MCAV/IMU integrated navigation algorithm, the coordinate system and coordinate transformation matrix are defined firstly. Relative geometrical relationship and coordinate system are illustrated in Fig. 2.

3.1. Landing site-fixed coordinate system (Σ^l)

The Landing site-fixed coordinate system $o_l - x_l y_l z_l$ is a local inertial frame with its origin centered at the predetermined landing site. The z_l-axis is aligned with the connection direction from the Mars geometrical center to the preselected landing site. The x_l-axis is orthogonal to z_l-axis and along the velocity direction of lander. The y_l-axis completes the right-handed orthogonal coordinate system. The lander's position, velocity and attitude parameters are all described in the landing site-fixed coordinate system.

3.2. Body-fixed coordinate system (Σ^b)

The origin of body-fixed coordinate system $o_b - x_b y_b z_b$ lies in the lander's mass center, three body axis of symmetry are defined as three coordinate axes x_b, y_b, z_b, respectively.

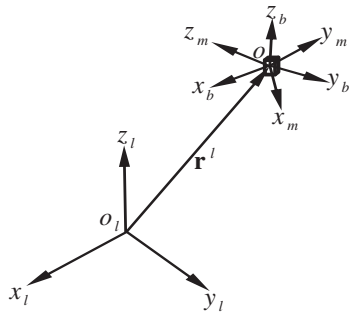

Fig. 2. Relative geometrical relationship and coordinate system.

3.3. MCAV-fixed coordinate system (Σ^m)

The origin of MCAV coordinate system $o_m - x_m y_m z_m$ lies in the MCAV's geometric center, three body axis of symmetry are defined as three coordinate axes x_m, y_m, z_m, respectively. The navigation measurement information (altitude and velocity) from MCAV is described in this coordinate system.

3.4. Installation matrix $\boldsymbol{T}_b^m$

The navigation sensor installation matrix $\mathbf{T}_b^m$ is defined to describe the orientation of MCAV in the body-fixed coordinate system. For simplify, the installation matrix $\mathbf{T}_b^m$ is assumed to be an identity matrix $\mathbf{I}_{3\times 3}$.

3.5. Coordinate transformation matrix $\boldsymbol{T}_l^b$

According to coordinate systems defined before, the coordinate transformation matrix $\mathbf{T}_l^b$ from the landing site-fixed coordinate system Σ^l to the body-fixed coordinate system Σ^b can be obtained as follows:

$$\begin{aligned}\mathbf{T}_l^b &= \begin{bmatrix}1 & 0 & 0\\ 0 & \cos\varphi & \sin\varphi\\ 0 & -\sin\varphi & \cos\varphi\end{bmatrix}\begin{bmatrix}\cos\theta & 0 & -\sin\theta\\ 0 & 1 & 0\\ \sin\theta & 0 & \cos\theta\end{bmatrix}\begin{bmatrix}\cos\psi & \sin\psi & 0\\ -\sin\psi & \cos\psi & 0\\ 0 & 0 & 1\end{bmatrix}\\ &= \begin{bmatrix}\cos\theta\cos\psi & \cos\theta\sin\psi & -\sin\theta\\ -\cos\varphi\sin\psi+\sin\varphi\sin\theta\cos\psi & \cos\varphi\cos\psi+\sin\varphi\sin\theta\sin\psi & \sin\varphi\cos\theta\\ \sin\varphi\sin\psi+\cos\varphi\sin\theta\cos\psi & -\sin\varphi\cos\psi+\cos\varphi\sin\theta\sin\psi & \cos\varphi\cos\theta\end{bmatrix},\end{aligned} \tag{1}$$

where ψ, θ, ϕ are the triaxial attitude angle, that is euler angle, and the rotation sequence $3(\psi) - 2(\theta) - 1(\phi)$ is adopted here.

3.6. Coordinate transformation matrix $\boldsymbol{T}_l^m$

According to the definitions aforementioned, the coordinate transformation matrix $\mathbf{T}_l^m$ from the landing site-fixed coordinate system Σ^l to the MCAV-fixed coordinate system Σ^m can be obtained as follows:

$$\mathbf{T}_l^m = \mathbf{T}_b^m \mathbf{T}_l^b. \tag{2}$$

4. Miniature Coherent Altimeter and Velocimeter (MCAV)

The MCAV is a significant advance over currently available alternatives, such as RADAR, image-correlation, and scanning direct-detection LIDAR, none of which fully addresses the needs of future Mars landers (Li, 2009; Chu et al., 2005). It features in one package:

(1) Low resource footprint (<1 Kg, <5 W per axis).
(2) Direct availability of three-axis rate vector and altitude.
(3) Velocity resolution to better than 10 cm/s.

(4) Small (<10 cm) beam footprint for terrain variation robustness.
(5) Small (<1°) and flexible fields of view (FOV) for ease of mechanical integration.
(6) High measurement-update rate (100 Hz).
(7) Non-scanning, physically robust package.

MCAV captures the inherent advantages of Doppler LIDAR (small beam footprint, small FOV and aperture, direct rate measurement) in a sensor with better performance, mass/power and robustness characteristics than previously possible. These advantages are primarily a small beam footprint, a small field of view and aperture, and direct, fast measurement of lander rate with respect to the ground. The key photonic component technology leveraged is the ultra-narrow linewidth, high power fiber laser.

The MCAV outputs can be easily reconstructed as follows:

$$\mathbf{c} = \begin{bmatrix} h \\ v_x \\ v_y \\ v_z \end{bmatrix}_m, \tag{3}$$

where h is the altitude measurement information and $[\,v_x \quad v_y \quad v_z\,]^T$ is the triaxial velocity measurement information. Subscript letter m stands for the MCAV-fixed coordinate system Σ^m.

5. Dynamic equations for Mars descent phase

Since dynamic equations are necessary to predict the states of Mars lander, the applicability of extended Kalman filter to combine the MCAV and IMU measurements rests on the availability of sufficiently accurate dynamic equations for Mars descent phase.

5.1. IMU model

The IMU of six degree-of-freedom measurement systems is designed to measure linear acceleration along three orthogonal axes and rotation rates around three orthogonal axes using three accelerometers and three axis gyros to make a complete six degree-of-freedom measurement of the dynamics. The acceleration and angular rate measured by the accelerometers and gyro, respectively, is represented as follows:

$$\begin{aligned} \tilde{\mathbf{a}} &= \mathbf{a} + \mathbf{b}_a + \boldsymbol{\xi}_a, \\ \tilde{\boldsymbol{\omega}} &= \boldsymbol{\omega} + \mathbf{b}_\omega + \boldsymbol{\xi}_\omega, \end{aligned} \tag{4}$$

where $\tilde{\mathbf{a}}$ is the linear accelerometer output along body axes, $\mathbf{a}$ is true linear acceleration, $\mathbf{b}_a$ is the acceleration bias, $\boldsymbol{\xi}_a$ is the white Gaussian acceleration output noise, $\tilde{\boldsymbol{\omega}}$ is the gyro output angular rate around body axes, $\boldsymbol{\omega}$ is the true angular rate, $\mathbf{b}_\omega$ is the angular rate bias, and $\boldsymbol{\xi}_\omega$ is the white Gaussian angular rate output noise.

5.2. Mars landing dynamics equations

In theory, the time development of the spacecraft position and attitude can be determined using detail dynamic models. However, dynamical modeling for Mars EDL includes many difficulties in establishing valid aerodynamic force and torque models, which lead to inaccurate dynamic models. In practice, autonomous spacecraft can directly use inertial reference units as dynamic models replacement. In the present implementation the linear acceleration and the angular velocity of the spacecraft are provided by accelerometer and gyro output data, respectively. The evolution of the spacecraft position and attitude state in time are obtained from the kinematics equations. The accelerometer and gyro biases are state variables and the accelerometer and gyro data are not considered as observations, therefore, the accelerometer and gyro noises are considered as state noise rather than as observation noise.

The landing dynamic equations are represented in landing site-fixed coordinate system as follows (Li et al., 2007):

$$\begin{aligned} \dot{\mathbf{r}} &= \mathbf{v}, \\ \dot{\mathbf{v}} &= \mathbf{T}_m^l(\tilde{\mathbf{a}} - \mathbf{b}_a - \boldsymbol{\xi}_a) + \mathbf{g}, \\ \dot{\mathbf{e}} &= \mathbf{K}(\tilde{\boldsymbol{\omega}} - \mathbf{b}_\omega - \boldsymbol{\xi}_\omega), \\ \dot{\mathbf{b}}_a &= \boldsymbol{\zeta}_a, \\ \dot{\mathbf{b}}_\omega &= \boldsymbol{\zeta}_\omega, \end{aligned} \tag{5}$$

where $\mathbf{r} = [r_1, r_2, r_3]^T$, $\mathbf{v} = [v_1, v_2, v_3]^T$, $\mathbf{e} = [\phi, \theta, \psi]^T$ are the position vector, velocity vector and triaxial euler angle vector. $\mathbf{T}_m^l = (\mathbf{T}_l^m)^{-1}$ is the coordinate transformation matrix from the MCAV-fixed coordinate system to the landing site-fixed coordinate system. $\mathbf{g}$ is the Mars gravity acceleration. $\boldsymbol{\omega} = [\,\omega_1 \quad \omega_2 \quad \omega_3\,]^T$ is the triaxial angle velocity described in the body-fixed coordinate system. Coefficient matrix $\mathbf{K}(\theta, \phi)$ is defined in the following Eq. (6). $\boldsymbol{\zeta}_a$ is white Gaussian noise of accelerometer first-order Markov process error and $\boldsymbol{\zeta}_\omega$ is white Gaussian noise of gyro first-order Markov process error.

$$\mathbf{K} = \frac{1}{\cos\theta} \begin{bmatrix} \cos\theta & \sin\theta\sin\varphi & \sin\theta\cos\varphi \\ 0 & \cos\theta\cos\varphi & -\cos\theta\sin\varphi \\ 0 & \sin\varphi & \cos\varphi \end{bmatrix}. \tag{6}$$

6. MCAV/IMU integrated navigation

In order to correct IMU constant bias, drift variation, scale factor errors, the velocity and altitude information from MCAV is combined with IMU measurement by use of extended Kalman filter.

6.1. Navigation measurement model

Recall the navigation measurement outputs from MCAV in Eq. (3). The inherent sensor properties produce the measurement noise. When measurement noise is pres-

ent, the navigation measurements are assumed to be modeled by

$$\mathbf{y} = \mathbf{c}(\mathbf{x}) + \boldsymbol{\upsilon}, \tag{7}$$

where

$$\mathbf{c}(\mathbf{x}) = \begin{bmatrix} r_3 \\ \mathbf{T}_l^m \mathbf{v} \end{bmatrix}_{4\times 1},$$

where $\mathbf{x}$ denotes the state variables of lander and is defined in the following Eq. (8). $r_3 = \mathbf{r}(3)$ and $\mathbf{v} = [v_1, v_2, v_3]^T$ are the third component of the position vector and the velocity vector, respectively, defined in the landing site-fixed coordinate system. The sensor noise $\boldsymbol{\upsilon}$ is modeled as zero mean white Gaussian process with covariance matrix of measurement errors $\mathbf{R}$.

6.2. Navigation filter design

In order to suppress navigation measurement noise and better estimate the state variables of lander, navigation filter is designed using extended Kalman filter.

Define state variables as follows:

$$\mathbf{x} = [\mathbf{r}^T, \mathbf{v}^T, \mathbf{e}^T, \mathbf{b}_a^T, \mathbf{b}_\omega^T]_{15\times 1}^T, \tag{8}$$

where the lander's relative position vector $\mathbf{r}$ and relative velocity vector $\mathbf{v}$, the attitude angle $\mathbf{e}$ are all defined with respect to the landing site-fixed coordinate system. At the same time, both acceleration bias $\mathbf{b}_a$ and angular rate bias $\mathbf{b}_\omega$, defined with respect to the body frame, are also considered as state variable.

Then, the Mars landing system dynamic equations can be rewritten as follows:

$$\dot{\mathbf{x}} = \mathbf{f}(\mathbf{x}) = \begin{bmatrix} \mathbf{v} \\ \mathbf{T}_m^l(\tilde{\mathbf{a}} - \mathbf{b}_a - \boldsymbol{\xi}_a) + \mathbf{g} \\ \mathbf{K}(\tilde{\boldsymbol{\omega}} - \mathbf{b}_\omega - \boldsymbol{\xi}_\omega) \\ \zeta_a \\ \zeta_\omega \end{bmatrix}_{15\times 1}. \tag{9}$$

The navigation filter can be designed using extended Kalman filter as follows:

Process equations:

$$\dot{\mathbf{x}}_k = \mathbf{f}(\mathbf{x}_{k-1}, \mathbf{w}_{k-1}). \tag{10}$$

Measurement equations:

$$\mathbf{y}(t_k) = \mathbf{c}(\mathbf{x}_k) + \boldsymbol{\upsilon}_k, \tag{11}$$

where the random variables $\mathbf{w}_k$ and $\boldsymbol{\upsilon}_k$ represent the state noise and measurement noise, respectively. They are assumed to be independent of each other, white noise and with normal probability distributions.

$$\begin{aligned} &p(\mathbf{w}) \sim N(0, \mathbf{Q}), \\ &p(\boldsymbol{\upsilon}) \sim N(0, \mathbf{R}), \end{aligned} \tag{12}$$

$$Cov\left[\mathbf{w}_k, \boldsymbol{\upsilon}_j\right] = E\left[\mathbf{w}_k \boldsymbol{\upsilon}_j^T\right] = 0. \tag{13}$$

Define state transfer matrix $\boldsymbol{\Phi}_{k/k-1}$:

$$\boldsymbol{\Phi}_{k/k-1} = \mathbf{I} + \mathbf{F}_{k/k-1} \cdot \Delta t, \tag{14}$$

$$\frac{d}{dt}\boldsymbol{\Phi}(t,\tau) = \mathbf{F}(t)\boldsymbol{\Phi}(t,\tau), \tag{15}$$

$$\boldsymbol{\Phi}(t,t) = \mathbf{I}, \tag{16}$$

where $\mathbf{F}$ is the Jacobian matrix of partial derivatives of $\mathbf{f}$ with respect to state variable $\mathbf{x}$, that is

$$\begin{aligned} \mathbf{F}_{k/k-1} &= \left.\frac{\partial \mathbf{f}(\mathbf{x}, k)}{\partial \mathbf{x}}\right|_{\mathbf{x}=\mathbf{x}_{k-1}} \\ &= \begin{bmatrix} \mathbf{0} & \mathbf{I}_{3\times 3} & \mathbf{0} & \mathbf{0} & \mathbf{0} \\ \mathbf{0} & \mathbf{0} & \frac{\partial \mathbf{T}_m^l(\tilde{\mathbf{a}}-\mathbf{b}_a-\boldsymbol{\xi}_a)}{\partial \mathbf{e}} & -\mathbf{T}_m^l & \mathbf{0} \\ \mathbf{0} & \mathbf{0} & \frac{\partial \mathbf{K}(\tilde{\boldsymbol{\omega}}-\mathbf{b}_\omega-\boldsymbol{\xi}_\omega)}{\partial \mathbf{e}} & \mathbf{0} & -\mathbf{K} \\ \mathbf{0} & \mathbf{0} & \mathbf{0} & \mathbf{0} & \mathbf{0} \\ \mathbf{0} & \mathbf{0} & \mathbf{0} & \mathbf{0} & \mathbf{0} \end{bmatrix}_{15\times 15}. \end{aligned} \tag{17}$$

The specific expression of $\frac{\partial \mathbf{T}_m^l(\tilde{\mathbf{a}}-\mathbf{b}_a-\boldsymbol{\xi}_a)}{\partial \mathbf{e}}$ and $\frac{\partial \mathbf{K}(\tilde{\boldsymbol{\omega}}-\mathbf{b}_\omega-\boldsymbol{\xi}_\omega)}{\partial \mathbf{e}}$ are rather complex and cumbersome, the detailed results can be found in the Appendix.

Define sensitivity matrix $\mathbf{H}_k$

$$\mathbf{H}_k = \left.\frac{\partial \mathbf{c}(\mathbf{x})}{\partial \mathbf{x}}\right|_{\mathbf{x}=\hat{\mathbf{x}}_k} = \begin{bmatrix} \frac{\partial \mathbf{r}(3)}{\partial \mathbf{x}} \\ \frac{\partial \mathbf{T}_l^m \mathbf{v}}{\partial \mathbf{x}} \end{bmatrix}_{4\times 15}. \tag{18}$$

According to vector differential calculus principle, the two differential components in Eq. (18) can be rewritten as more simple form

$$\begin{aligned} \frac{\partial \mathbf{r}(3)}{\partial \mathbf{x}} &= \left[\frac{\partial \mathbf{r}(3)}{\partial \mathbf{r}^T}, \frac{\partial \mathbf{r}(3)}{\partial \mathbf{v}^T}, \frac{\partial \mathbf{r}(3)}{\partial \mathbf{e}^T}, \frac{\partial \mathbf{r}(3)}{\partial \mathbf{b}_a^T}, \frac{\partial \mathbf{r}(3)}{\partial \mathbf{b}_\omega^T}\right] \\ &= \left[\frac{\partial \mathbf{r}(3)}{\partial \mathbf{r}^T}, \mathbf{0}_{1\times 3}, \mathbf{0}_{1\times 3}, \mathbf{0}_{1\times 3}, \mathbf{0}_{1\times 3}\right]_{1\times 15}, \end{aligned} \tag{19}$$

$$\begin{aligned} \frac{\partial \mathbf{T}_l^m \mathbf{v}}{\partial \mathbf{x}} &= \left[\frac{\partial \mathbf{T}_l^m \mathbf{v}}{\partial \mathbf{r}^T}, \frac{\partial \mathbf{T}_l^m \mathbf{v}}{\partial \mathbf{v}^T}, \frac{\partial \mathbf{T}_l^m \mathbf{v}}{\partial \mathbf{e}^T}, \frac{\partial \mathbf{T}_l^m \mathbf{v}}{\partial \mathbf{b}_a^T}, \frac{\partial \mathbf{T}_l^m \mathbf{v}}{\partial \mathbf{b}_\omega^T}\right] \\ &= \left[\mathbf{0}_{3\times 3}, \mathbf{T}_l^m, \frac{\partial \mathbf{T}_l^m \mathbf{v}}{\partial \mathbf{e}^T}, \mathbf{0}_{3\times 3}, \mathbf{0}_{3\times 3}\right]_{3\times 15}, \end{aligned} \tag{20}$$

where

$$\frac{\partial \mathbf{r}(3)}{\partial \mathbf{r}^T} = [\,0 \quad 0 \quad 1\,].$$

Because the installation matrix $\mathbf{T}_b^m$ is constant matrix, the expression of $\frac{\partial \mathbf{T}_l^m \mathbf{v}}{\partial \mathbf{e}^T}$ can be further simplified as follows:

$$\frac{\partial \mathbf{T}_l^m \mathbf{v}}{\partial \mathbf{e}^T} = \frac{\partial \mathbf{T}_b^m \mathbf{T}_l^b \mathbf{v}}{\partial \mathbf{e}^T} = \mathbf{T}_b^m \frac{\partial \mathbf{T}_l^b \mathbf{v}}{\partial \mathbf{e}^T}. \tag{21}$$

The specific expression of $\frac{\partial \mathbf{T}_l^b \mathbf{v}}{\partial \mathbf{e}^T}$ can be also given out in the Appendix.

Initialization: For $k = 0$, set

$$\hat{\mathbf{x}}_0 = E[\mathbf{x}_0], \tag{22}$$

$$\mathbf{P}_0 = E\left[(\mathbf{x}_0 - E[\mathbf{x}_0])(\mathbf{x}_0 - E[\mathbf{x}_0])^T\right]. \tag{23}$$

EKF time update

$$\dot{\hat{\mathbf{x}}}_{k/k-1} = \mathbf{f}(k, \hat{\mathbf{x}}_{k-1}), \tag{24}$$

$$\mathbf{P}_{k/k-1} = \mathbf{\Phi}_{k/k-1}\mathbf{P}_{k-1}\mathbf{\Phi}^T_{k/k-1} + \mathbf{Q}_{k-1}. \tag{25}$$

EKF measurement update

$$\mathbf{K}_k = \mathbf{P}_{k/k-1}\mathbf{H}^T_k[\mathbf{H}_k\mathbf{P}_{k/k-1}\mathbf{H}^T_k + \mathbf{R}_k]^{-1}, \tag{26}$$

$$\widehat{\mathbf{x}}_{k/k} = \widehat{\mathbf{x}}_{k/k-1} + \mathbf{K}_k\big[\mathbf{y}(t_k) - \mathbf{c}(\hat{\mathbf{x}}_{k/k-1})\big], \tag{27}$$

$$\mathbf{P}_k = (\mathbf{I} - \mathbf{K}_k\mathbf{H}_k)\mathbf{P}_{k/k-1}. \tag{28}$$

7. Simulation results

In order to confirm the validity of MCAV/IMU integrated navigation algorithm proposed in this paper, simulation in MATLAB/Simulink environment has been carried out. Fig. 3 shows the simulation blocks built in MATLAB/Simulink environment. Dynamic model block, including accuracy landing dynamic model and tracking guidance law, provides the referenced state variables for MCAV navigation measurement construction and navigation error analysis. Navigation measurement block outputs the altitude and triaxial velocity information according to the inputted referenced state variables and the Eq. (7). Navigation filter block is set up based on filter iterative computation, which performs MCAV and IMU integrated navigation algorithm. MCAV/IMU integrated navigation errors and IMU based Dead Reckoning navigation errors are analyzed contrastively in the navigation error block.

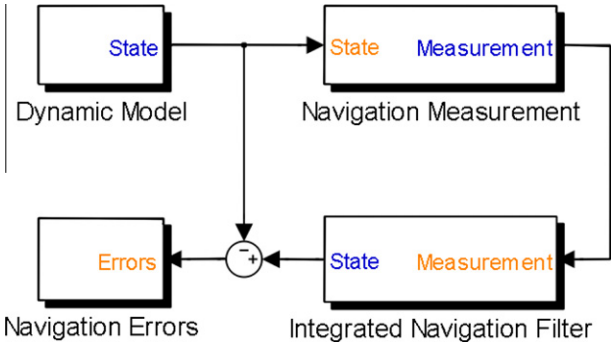

Fig. 3. Simulink block diagram (Matlab/Simulink blocks).

Table 1
Specifications of Crossbow IMU-300CB.

Update rate (Hz)	>100 (Hz)
Triaxial Gyro	
Range (°/s)	±100
Bias (°/s)	±2.0
Scale factor accuracy (%)	<1
Non-linearity (%FS)	<0.3
Resolution (°/s)	<0.05
Random walk (°/min)	<0.85
Triaxial accelerometer	
Range (g)	±2
Bias (mg)	<±30
Scale factor accuracy (%)	<1
Non-linearity (%FS)	<1
Resolution (mg)	<1.0
Random walk (m/s/min)	<0.15

The bias and standard deviation of noise of accelerometer and gyro applying to the measurement simulation are selected based on the specification of Crossbow IMU-300CB in Table 1 (Crossbow Technology Inc., 1999). For implementation of the MCAV/IMU integrated EKF, it was assumed that the IMU performance was as shown in Table 2. The initial state parameters of lander are described in Table 3 and navigation filter parameters are defined in Table 4. To demonstrate the good convergence property of MCAV/IMU integrated EKF algorithm, the values of state error covariance matrix are deliberately set relatively

Table 2
Acceleration and gyro error specifications for IMU used in the simulation.

	Bias	White noise (Std.)	Bias noise (Std.)
Acceleration error (m/s^2)			
x-axis	$0.3\cos(t/100)$	1.0×10^{-3}	1.0×10^{-8}
y-axis	$0.3\cos(t/200)$	1.0×10^{-3}	1.0×10^{-8}
z-axis	$0.3\sin(t/100)$	1.0×10^{-3}	1.0×10^{-8}
Gyro error (°/s)			
x-axis	$2\sin(t/100)$	1.0×10^{-3}	1.0×10^{-8}
y-axis	$2\sin(t/200)$	1.0×10^{-3}	1.0×10^{-8}
z-axis	$2\cos(t/100)$	1.0×10^{-3}	1.0×10^{-8}

Table 3
Initial state parameters $\mathbf{x}_0$.

Initial state parameters	
$r_x\ r_y\ r_z$	[−80 −1000 5000] (m)
$v_x\ v_y\ v_z$	[0 20 −150] (m/s)
$\varphi\ \theta\ \psi$	[0 0 0.5286] (rad)
ω_0	[0 0 −0.003776] (rad/s)
$\mathbf{b}_a$	[0.3 0.3 0] (m/s^2)
$\mathbf{b}_\omega$	[0 0 0.0349] (rad/s)

Table 4
MCAV/IMU integrated Navigation filter parameters.

Error covariance matrix

$$P_0 \quad \begin{bmatrix} 4\times10^4\mathbf{I}_{3\times3} & & & & \\ & 4\times10^2\mathbf{I}_{3\times3} & & & \\ & & 2.7\times10^{-3}\mathbf{I}_{3\times3} & & \\ & & & 10^{-16}\mathbf{I}_{3\times3} & \\ & & & & 10^{-16}\mathbf{I}_{3\times3} \end{bmatrix}_{15\times15}$$

Measurement noise covariance matrix

$$R_k \quad 10^{-2}\mathbf{I}_{4\times4}$$

Covariance matrix of process

$$Q \quad \begin{bmatrix} \mathbf{0}_{3\times3} & & & & \\ & 10^{-6}\mathbf{I}_{3\times3} & & & \\ & & 10^{-6}\mathbf{I}_{3\times3} & & \\ & & & 10^{-16}\mathbf{I}_{3\times3} & \\ & & & & 10^{-16}\mathbf{I}_{3\times3} \end{bmatrix}_{15\times15}$$

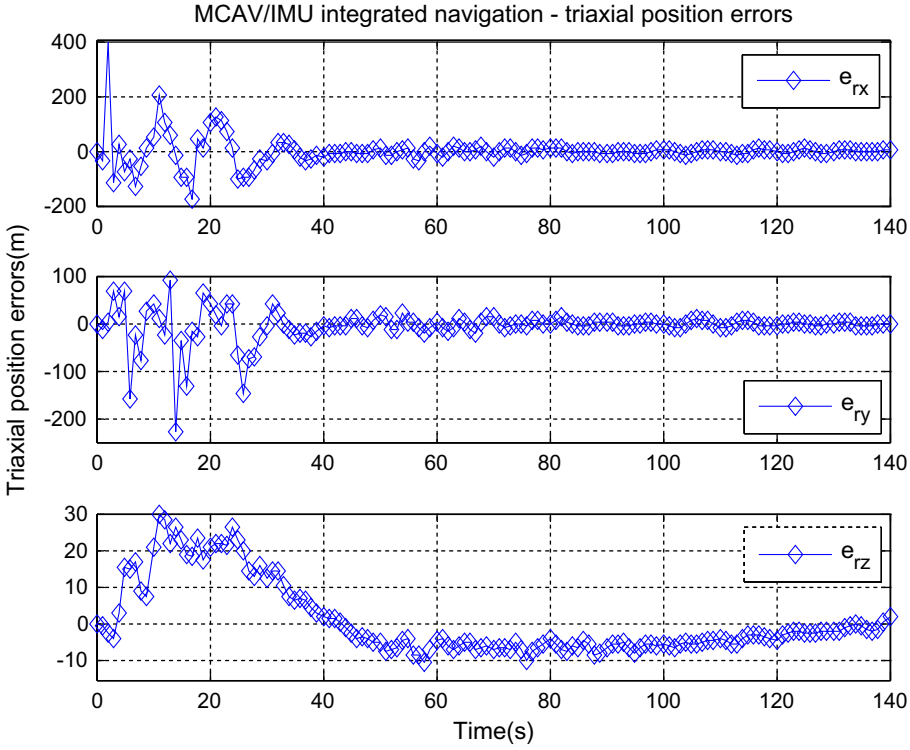

Fig. 4. Triaxial position errors of MCAV/IMU integrated navigation.

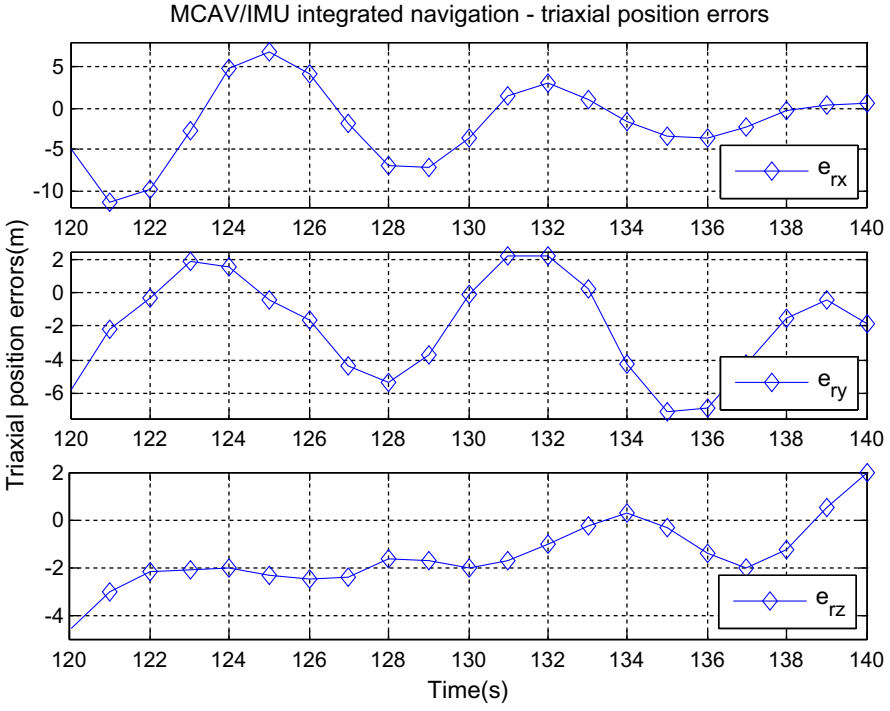

Fig. 5. Triaxial position errors of MCAV/IMU integrated navigation between 120 and 140 s.

large in the simulation. The planned landing span is supposed to be 140 s and the Mars gravity acceleration is assumed to be a constant $g = [0, 0, -3.69]^T m/s^2$. Simulation sample period/step is set to one second and four-order Runge–Kutta is selected as numerical solver of integral Eq. (10).

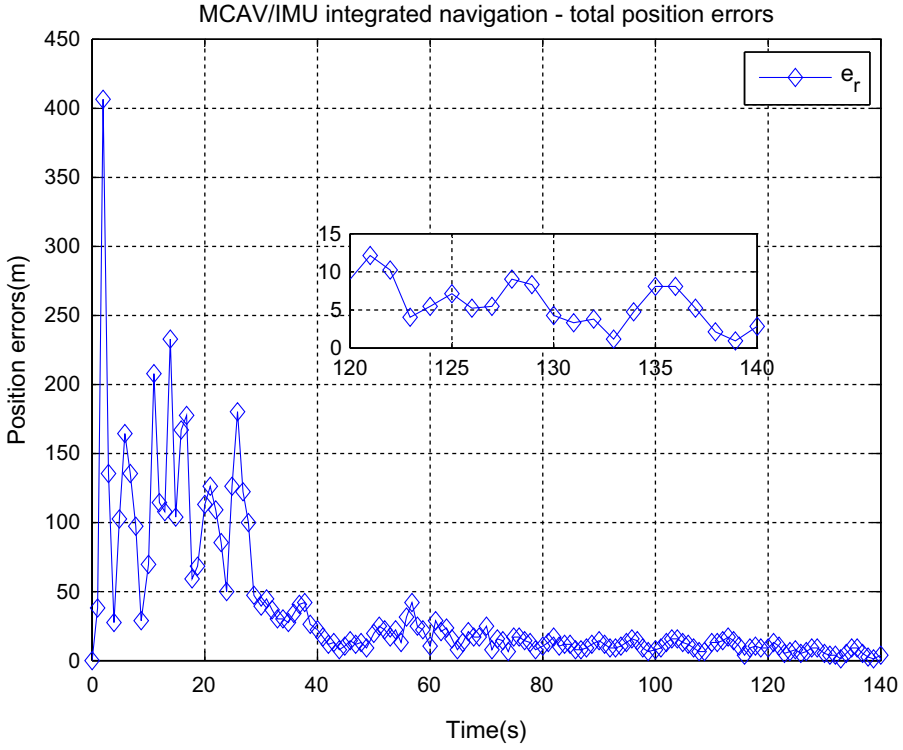

Fig. 6. Total position errors of MCAV/IMU integrated navigation.

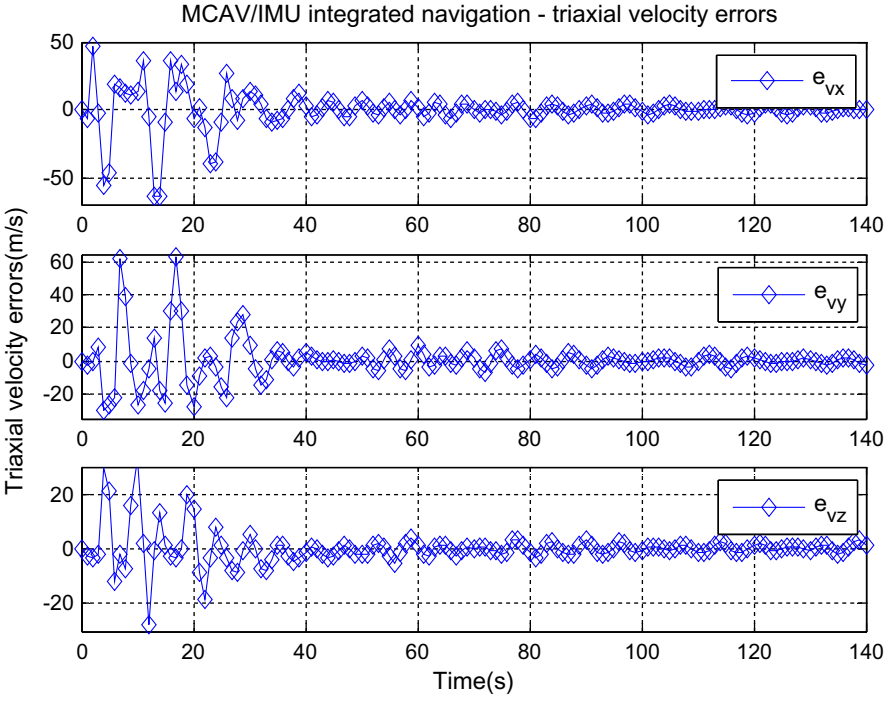

Fig. 7. Triaxial velocity errors of MCAV/IMU integrated navigation.

The difference between the referenced state variables of lander and estimated state variables, that is navigation errors, are plotted in Figs. 4–15. Triaxial position errors and total position errors from MCAV/IMU integrated navigation are shown in Figs. 4 and 6 and triaxial velocity errors and total velocity errors from MCAV/IMU integrated navigation are also plotted in Figs. 7 and 9. Figs. 5 and 8 depicted the partially amplified figures of

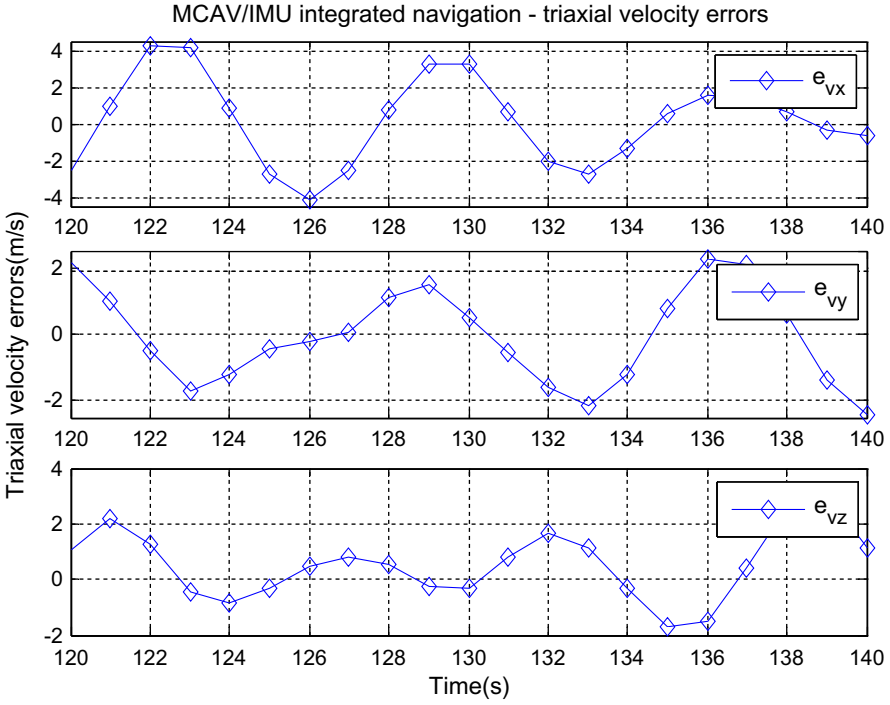

Fig. 8. Triaxial velocity errors of MCAV/IMU integrated navigation between 120 and 140 s.

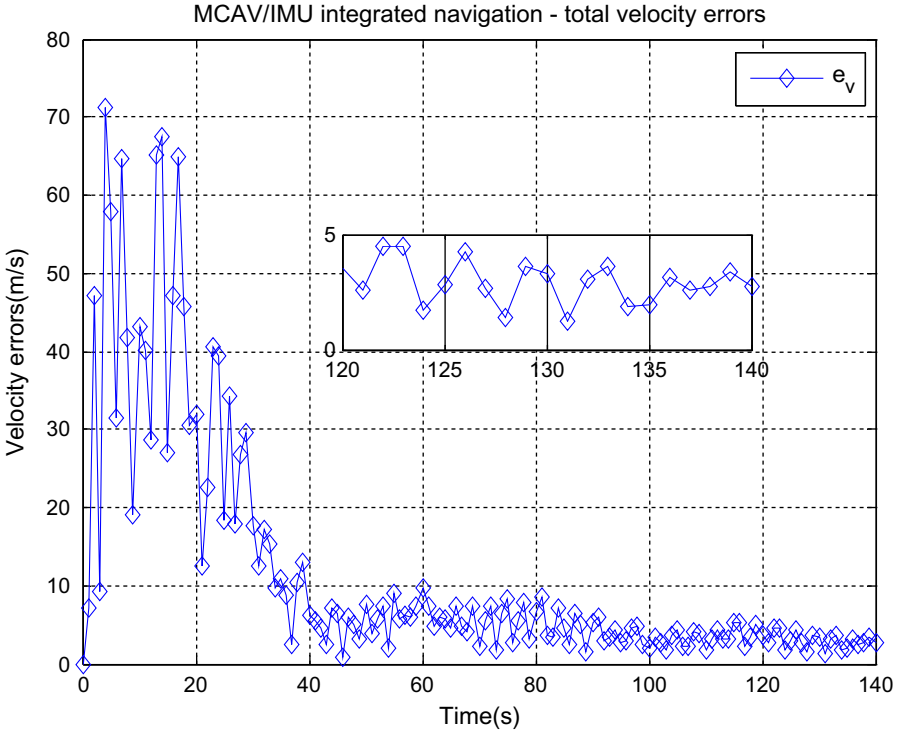

Fig. 9. Total velocity errors of MCAV/IMU integrated navigation.

the triaxial position errors and velocity errors form MCAV/IMU integrated navigation between 120 and 140 s, respectively. Based on the simulation results showed in Figs. 4–9, it is concluded that the filter convergence of MCAV/IMU integrated navigation is quite good and the navigation accuracy is fairly high with position errors less than 10 m and velocity errors less than 5 m/s, which can meet the need of pin-point Mars landing missions. At the same time, it also should be noticed that the z-axis position error and velocity error converge faster to a relatively small

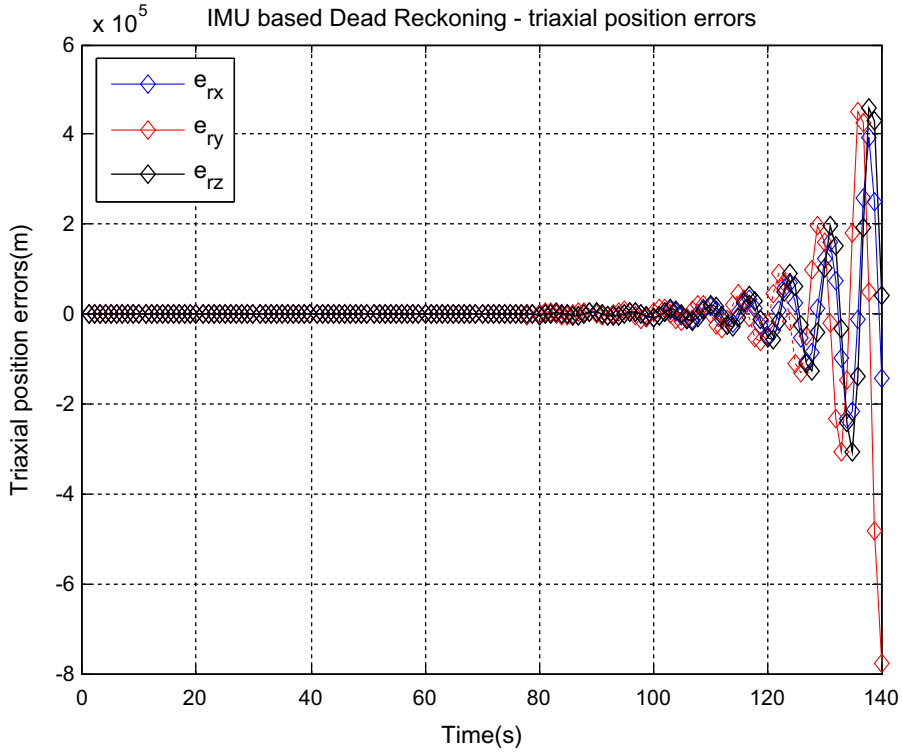

Fig. 10. Triaxial position errors of IMU based Dead Reckoning.

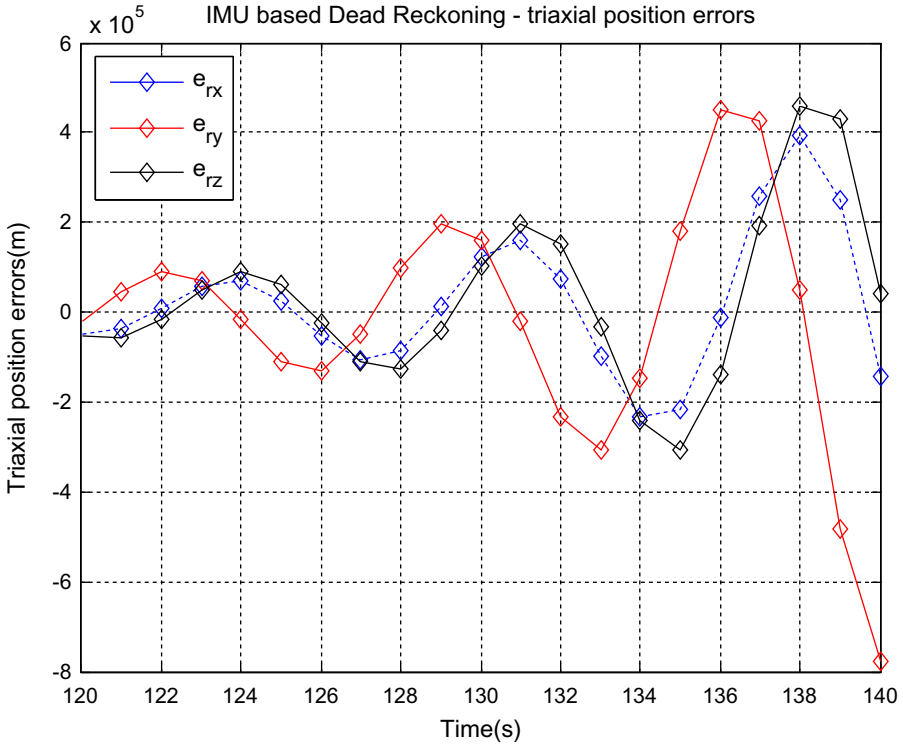

Fig. 11. Triaxial position errors of IMU based Dead Reckoning between 120 and 140 s.

magnitude than the other two axial errors. The reason why z-axis errors have better convergence than the others lies in navigation sensor MCAV only provides the range information (attitude) along the z-axis.

When Kalman filter gain matrix is set to zero ($\mathbf{K}_k = 0$), MCAV/IMU integrated navigation is degraded to IMU based Dead Reckoning navigation. Triaxial position errors and total position errors from IMU based Dead Reckoning

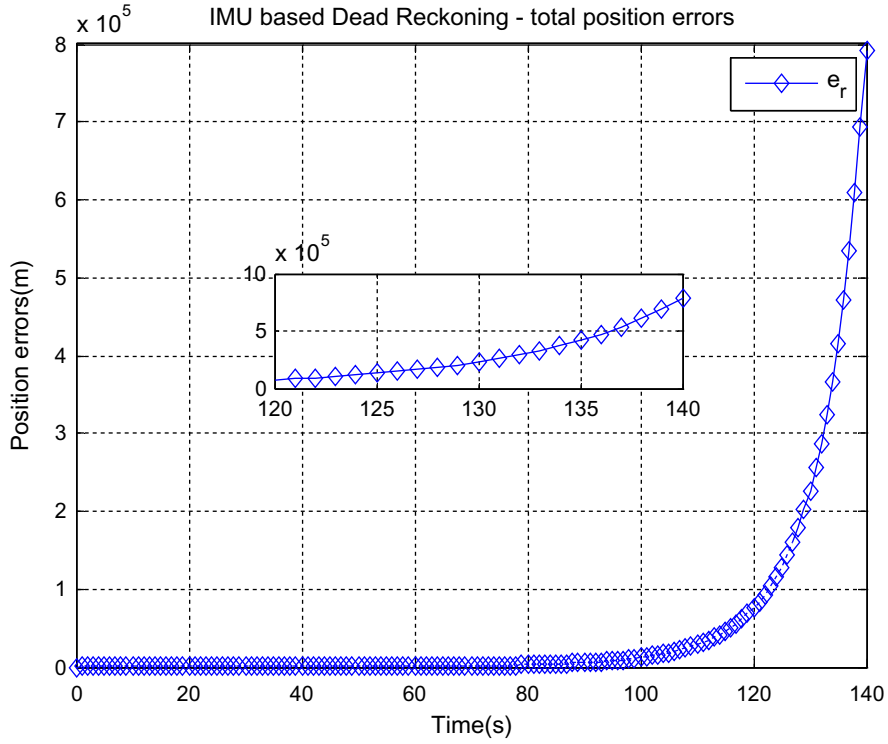

Fig. 12. Total position errors of IMU based Dead Reckoning.

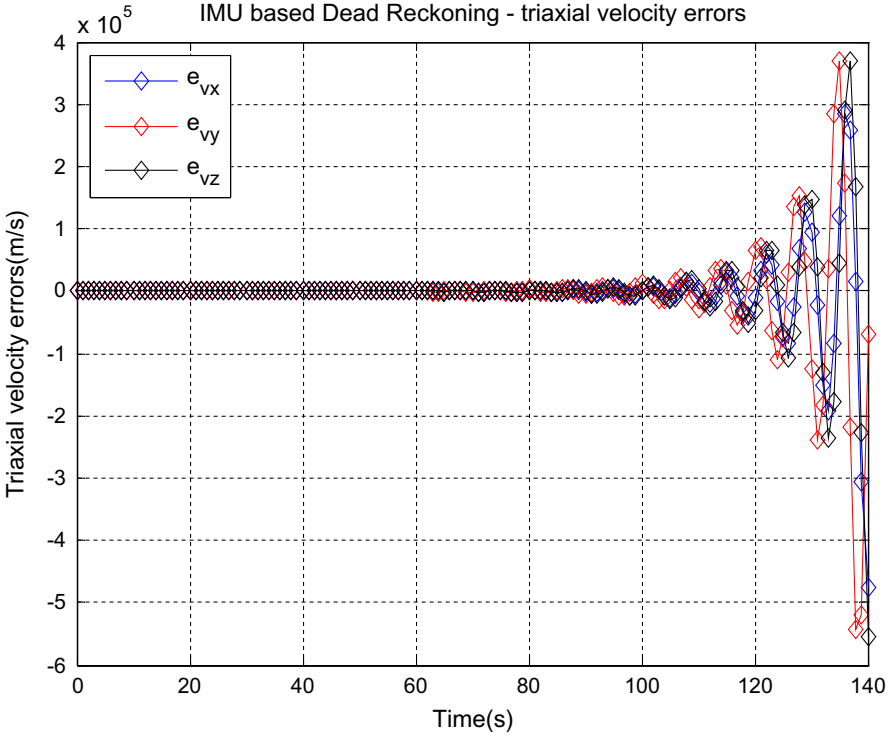

Fig. 13. Triaxial velocity errors of IMU based Dead Reckoning.

navigation are plotted in Figs. 10 and 12 and triaxial velocity errors and total velocity errors from IMU based Dead Reckoning navigation are shown in Figs. 13 and 15. Figs. 11 and 14 depicted the partially amplified figures of the triaxial position errors and velocity errors form IMU based Dead Reckoning navigation between 120 and 140 s,

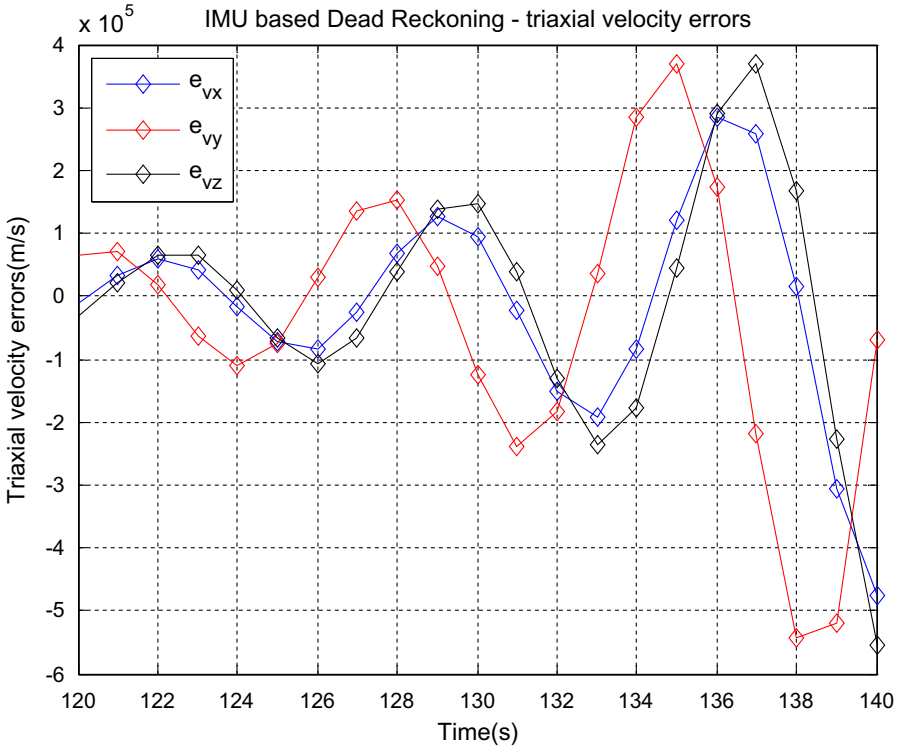

Fig. 14. Triaxial velocity errors of IMU based Dead Reckoning between 120 and 140 s.

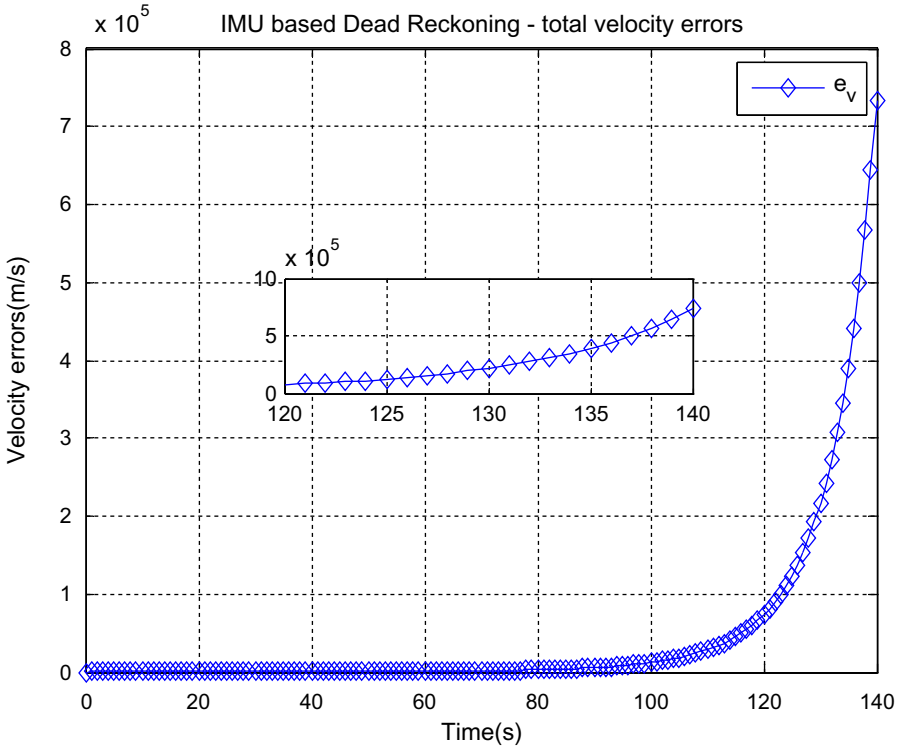

Fig. 15. Total velocity errors of IMU based Dead Reckoning.

respectively. It is easily concluded from the above simulation results shown in Figs. 10–15 that the navigation outputs from IMU based Dead Reckoning navigation gradually diverge and the final position errors reach the magnitude of several hundred kilometers under the current simulation assumptions. Because the bias terms of IMU have been corrected by use of the altitude and velocity information from MCAV, the accuracy of MCAV/IMU

integrated navigation has been greatly improved compared to IMU based Dead Reckoning navigation.

8. Conclusion

This paper proposes and implements the MCAV/IMU integrated navigation for the descent phase of Mars EDL. The altitude and velocity information from navigation sensor MCAV is used to correct the bias and drift of inertial measurement unit by extended Kalman filter technique. Simulation results imply the accuracy of MCAV/IMU integrated navigation has been greatly improved compared to IMU based Dead Reckoning navigation and satisfies the need of future pin-point Mars landing missions. In current work, we assume that guidance control produces no errors in order to analyze the navigation errors clearly. The landing position and velocity errors, including both the navigation errors and guidance control errors, will be analyzed in the farther study.

Acknowledgements

The work described in this paper was supported by the National Natural Science Foundation of China (Grant No. 60804057), China Postdoctoral Science Foundation Funded Project (Grant No. 20090450148), Ph.D. Programs Foundation of Ministry of Education of China (Grant No. 200802871031) and Jiangsu Planned Projects for Postdoctoral Research Funds (Grant No. 0901037C).

Appendix A

I. In the context, the installation matrix $\mathbf{T}_m^b$ is assumed to be an identity matrix $\mathbf{I}_{3\times3}$, then we can easily obtain $\frac{\partial \mathbf{T}_m^l(\widetilde{\mathbf{a}}-\mathbf{b}_a-\boldsymbol{\xi}_a)}{\partial \mathbf{e}} = \frac{\partial \mathbf{T}_b^l(\widetilde{\mathbf{a}}-\mathbf{b}_a-\boldsymbol{\xi}_a)}{\partial \mathbf{e}}$.

Define a_i, $i = 1, 2, 3$ is the ith element of the true linear acceleration vector $\mathbf{a} = (\tilde{\mathbf{a}} - \mathbf{b}_a - \boldsymbol{\xi}_a)$, then the detail expression of $\frac{\partial \mathbf{T}_m^l(\widetilde{\mathbf{a}}-\mathbf{b}_a-\boldsymbol{\xi}_a)}{\partial \mathbf{e}}$ can be obtained as follows:

$$\frac{\partial \mathbf{T}_m^l(\tilde{\mathbf{a}}-\mathbf{b}_a-\boldsymbol{\xi}_a)}{\partial \mathbf{e}} = \frac{\partial \mathbf{T}_b^l(\tilde{\mathbf{a}}-\mathbf{b}_a-\boldsymbol{\xi}_a)}{\partial \mathbf{e}} \triangleq \begin{bmatrix} \mathbb{C}_{11} & \mathbb{C}_{12} & \mathbb{C}_{13} \\ \mathbb{C}_{21} & \mathbb{C}_{22} & \mathbb{C}_{23} \\ \mathbb{C}_{31} & \mathbb{C}_{32} & \mathbb{C}_{33} \end{bmatrix}_{3\times3},$$

where

$\mathbb{C}_{11} = (\sin\varphi\sin\psi + \cos\varphi\sin\theta\cos\psi)a_2 + (\cos\varphi\sin\psi - \sin\varphi\sin\theta\cos\psi)a_3$
$\mathbb{C}_{12} = -\sin\theta\cos\psi a_1 + \sin\varphi\cos\theta\cos\psi a_2 + \cos\varphi\cos\theta\cos\psi a_3$
$\mathbb{C}_{13} = \cos\theta\sin\psi a_1 + (-\cos\varphi\cos\psi - \sin\varphi\sin\theta\cos\psi)a_2 + (\sin\varphi\sin\psi - \cos\varphi\sin\theta\sin\psi)a_3$
$\mathbb{C}_{21} = (-\sin\varphi\cos\psi + \cos\varphi\sin\theta\sin\psi)a_2 + (-\cos\varphi\cos\psi - \sin\varphi\sin\theta\sin\psi)a_3$
$\mathbb{C}_{22} = -\sin\theta\sin\psi a_1 + \sin\varphi\cos\theta\sin\psi a_2 + \cos\varphi\cos\theta\sin\psi a_3$
$\mathbb{C}_{23} = \cos\theta\cos\psi a_1 + (-\cos\varphi\sin\psi + \sin\varphi\sin\theta\cos\psi)a_2 + (\sin\varphi\sin\psi + \cos\varphi\sin\theta\cos\psi)a_3$
$\mathbb{C}_{31} = \cos\varphi\cos\theta a_2 - \sin\varphi\cos\theta a_3$
$\mathbb{C}_{32} = -\cos\theta a_1 - \sin\varphi\sin\theta a_2 - \cos\varphi\sin\theta a_3$
$\mathbb{C}_{33} = 0.$

II. Define ω_i, $i = 1, 2, 3$ is the ith element of the true angular rate vector $\boldsymbol{\omega} = (\tilde{\boldsymbol{\omega}} - \mathbf{b}_\omega - \boldsymbol{\xi}_\omega)$, then the detail expression of $\frac{\partial \mathbf{K}(\tilde{\boldsymbol{\omega}}-\mathbf{b}_\omega-\boldsymbol{\xi}_\omega)}{\partial \mathbf{e}}$ can be obtained as follows:

$$\frac{\partial \mathbf{K}(\tilde{\boldsymbol{\omega}}-\mathbf{b}_\omega-\boldsymbol{\xi}_\omega)}{\partial \mathbf{e}} \triangleq \begin{bmatrix} \mathbb{Q}_{11} & \mathbb{Q}_{12} & \mathbb{Q}_{13} \\ \mathbb{Q}_{21} & \mathbb{Q}_{22} & \mathbb{Q}_{23} \\ \mathbb{Q}_{31} & \mathbb{Q}_{32} & \mathbb{Q}_{33} \end{bmatrix}_{3\times3},$$

where $\mathbb{Q}_{11} = (\cos\varphi\omega_2 - \sin\varphi\omega_3)\sin\theta/\cos\theta$

$\mathbb{Q}_{12} = (\sin\varphi\omega_2 + \cos\varphi\omega_3)/(\cos\theta)^2$
$\mathbb{Q}_{13} = 0$
$\mathbb{Q}_{21} = -\sin\varphi\omega_2 - \cos\varphi\omega_3$
$\mathbb{Q}_{23} = 0$
$\mathbb{Q}_{31} = (\cos\varphi\omega_2 - \sin\varphi\omega_3)/\cos\theta$
$\mathbb{Q}_{32} = (\sin\varphi\omega_2 + \cos\varphi\omega_3)\sin\theta/(\cos\theta)^2$
$\mathbb{Q}_{33} = 0.$

III. Define v_i, $i = 1, 2, 3$ is the ith element of the velocity vector v, then the detail expression of $\frac{\partial \mathbf{T}_l^b \mathbf{v}}{\partial \mathbf{e}^T}$ can be obtained as follows:

$$\frac{\partial \mathbf{T}_l^b \mathbf{v}}{\partial \mathbf{e}^T} \triangleq \begin{bmatrix} \mathbb{R}_{11} & \mathbb{R}_{12} & \mathbb{R}_{13} \\ \mathbb{R}_{21} & \mathbb{R}_{22} & \mathbb{R}_{23} \\ \mathbb{R}_{31} & \mathbb{R}_{32} & \mathbb{R}_{33} \end{bmatrix}_{3\times3},$$

where $\mathbb{R}_{11} = 0$

$\mathbb{R}_{12} = -\sin\theta\cos\psi v_1 - \sin\theta\sin\psi v_2 - \cos\theta v_3$
$\mathbb{R}_{13} = -\cos\theta\sin\psi v_1 + \cos\theta\cos\psi v_2$
$\mathbb{R}_{21} = (-\sin\varphi\cos\psi + \cos\varphi\sin\theta\sin\psi)v_2 + \cos\varphi\cos\theta v_3$
$\mathbb{R}_{22} = \sin\varphi\cos\theta\cos\psi v_1 + \sin\varphi\cos\theta\sin\psi v_2 - \sin\varphi\sin\theta v_3$
$\mathbb{R}_{23} = -(\cos\varphi\cos\psi + \sin\varphi\sin\theta\sin\psi)v_1 + (-\cos\varphi\sin\psi + \sin\varphi\sin\theta\cos\psi)v_2$
$\mathbb{R}_{31} = (\cos\varphi\sin\psi - \sin\varphi\sin\theta\cos\psi)v_1 + (-\cos\varphi\cos\psi - \sin\varphi\sin\theta\sin\psi)v_2 - \sin\varphi\cos\theta v_3$
$\mathbb{R}_{32} = \cos\varphi\cos\theta\cos\psi v_1 + \cos\varphi\cos\theta\sin\psi v_2 - \cos\varphi\sin\theta v_3$
$\mathbb{R}_{33} = (\sin\varphi\cos\psi - \cos\varphi\sin\theta\sin\psi)v_1 + (\sin\varphi\sin\psi + \cos\varphi\sin\theta\cos\psi)v_2.$

References

Alain, P., Christian, P. Validation and verification approach for European safe precision landing guidance, Navigation and Control (GNC) Technologies, in: Sixth International Planetary Probe Workshop, 2008.

Benjamin, A.L., Bolen, S.M., Smit, G.N., Cuseo, J.A., Lindell, S.D. Overview: precision landing/hazard avoidance concepts and MEMS

technology insertion for human Mars lander missions, in: AIAA/IEEE Digital Avionics Systems Conference, IEEE Proceedings, vol. 2. pp. 18–25, 1997.

Brand, T., Fuhrman, L., Geller, D., Hattis, P., Paschall, S., Tao, Y.C. GN&C technology needed to achieve pinpoint landing accuracy at Mars, in: AIAA/AAS Astrodynamics Specialist Conference and Exhibit, Providence, Rhode Island, August 16–19. AIAA 2004-4748, 2004.

Braun, R., Manning, R. Mars exploration entry, descent, and landing challenges. Journal of Spacecraft and Rockets 44 (2), 310–323, 2007.

Burkhart, P.D., Bishop, R.H., Crain, T.P. Integrated navigation and guidance for precision landing at Mars, in: International Symposium on Space Flight Dynamics. Pasadena, CA, USA, 3rd December, 2001.

Cheng, C.C. Development of advanced entry, descent, and landing technologies for future Mars missions, in: 2006 IEEE Aerospace Conference, pp. 1–8, 2006.

Chu, C.-C., Hayati, S.A., Udomkesmalee, S., Lavery, D.B. Mars base technology program overview. Space 2005, Long Beach, California, August 30–1, AIAA-2005-6744, 2005.

Crossbow Technology Inc., "Crossbow DMU User's Manual", <www.xbow.com>, San Jose, CA, 1999.

Guizzo, G.P., Bertoli, A., Torre, A.D., Magistrati, G., Mailland, F., Vukman, I., Philippe, C., Jurado, M.M., Ori, G.G., Macdonald, M., Romberg, O., Debei, S., Zaccariotto, M. Mars and Moon exploration passing through the European precision landing GNC test facility. Acta Astronautica 63 (1-4), 74–90, 2007.

Korzun, A.M., Dubos, G.F., Iwata, C.K., Stahl, B.A., Quicksall, J.J. A concept for the entry, descent and, landing of high-mass payloads at Mars. Acta Astronautica, doi:10.1016/j.actaastro.2009.10.003, 2009.

Li, S., Zhang, L., Peng, Y.M. Feasibility study for China Mars return mission after "YH-1", Inner technical report, CAST/NUAA, 2009-7.

Li, S., Zhang, L. Autonomous navigation and guidance scheme for precise and safe planetary landing. Aircraft Engineering and Aerospace Technology: An International Journal 81 (6), 516–521, 2009.

Li, S., Cui, P.Y., Cui, H.T. Vision-aided inertial navigation for pinpoint planetary landing. Aerospace Science and Technology 11 (6), 499–506, 2007.

Parkes, S.M., Silva, V. GNC sensors for planetary landers – a review. European Space Agency, (Special Publication) ESA SP (509), 744–752, 2001.

Parreira, B., Rogata, P., Di Sotto, E., Caramagno, A., Rebordão, J.M., Motrena, P., Mancuso, S. Consolidated performance assessment of hazard avoidance techniques for vision based landing, in: AIAA Guidance, Navigation, and Control Conference, pp. 5163–5178, 2007.

Rogata, P., Di Sotto, E., Câmara, F., Caramagno, A., Rebordão, J.M., Correia, B., Duarte, P., Mancuso, S. Design and performance assessment of hazard avoidance techniques for vision-based landing. Acta Astronautica 61 (1-6), 63–77, 2007.

Singh, G., SanMartin, A.M., Wong, E.C. Guidance and control design for powered descent and landing on Mars, in: IEEE Aerospace Conference, pp. 1–8, 2007.

Steltzner, A., Kipp, D., Chen, A., Burkhart, D., Guernsey, C., Mendeck, G., Mitcheltree, R., Powell, R., Rivellini, T., San Martin, M., Way, D. Mars science laboratory: entry, descent, and landing system, in: IEEE Aerospace Conference, pp. 1–15, 2006.

Striepe, S.A., Way, D.W., Dwyer, A.M., Balaram, J. Mars science laboratory simulations for entry, descent, and landing. Journal of Spacecraft and Rockets 43 (2), 311–323, 2006.

Way, D.W., Powell, R.W., Chen, A., Steltzner, A.D., Martin, A.M.S., Burkhart, P.D., Mendeck, G.F. Mars science laboratory: entry, descent, and landing system performance, in: 2007 IEEE Aerospace Conference, pp. 871–889, 2007.

Wolf, A.A., Graves, C., Powell, R., Johnson, W. Systems for pinpoint landing at Mars. Advance in the Astronautical Sciences 119, 2677–2696, 2005.